npj | 2D materials and applications

Article

Published in partnership with FCT NOVA with the support of E-MRS

https://doi.org/10.1038/s41699-024-00515-3

First-principles study of the magneto-Raman effect in van der Waals layered magnets

Xiangru Kong [1,2] ✉, Panchapakesan Ganesh[2] & Liangbo Liang[2] ✉

Magneto-Raman spectroscopy has been used to study spin-phonon coupling in two-dimensional (2D) magnets. Raman spectra of CrI_3 show a strong dependence on the magnetic order within a layer and between the layers. Here we carry out the first systematic theoretical investigation of the magneto-Raman effect in 2D magnets by performing density functional theory calculations and developing a generalized polarizability model. Our first-principles simulations well reproduce experimental Raman spectra of CrI_3 with different magnetic states. The model reveals how the change of spin orientation in each layer is coupled to the layer's vibration to induce or eliminate the spin-dependent anti-symmetric off-diagonal terms in the Raman tensor for altering the selection rules. We also uncover that the correlation between phonon modes and magnetic orders is a universal phenomenon, which should exist in other phonon modes and 2D magnets. Our predictive simulations and modeling are expected to guide the research in 2D magnets.

Magnetism in two-dimensional (2D) van der Waals (vdW) layered materials has attracted much attention due to the fascinating physics and potential applications[1–4]. CrI_3 is among the first 2D magnets to be discovered that exhibit spontaneous out-of-plane ferromagnetism in the monolayer limit[1]. A characteristic feature of 2D materials is that the intralayer bonding is strong while the interlayer coupling is weak and typically dominated by vdW interactions. Such a contrast gives rise to an interesting phenomenon that the intralayer magnetic order cannot be easily altered, but the spin orientations between the layers can be relatively easily manipulated between ferromagnetic (FM) and antiferromagnetic (AFM) orders by various methods such as interlayer stacking sliding/rotation[5,6] and applying an electric/magnetic field[7–9]. The manipulation of interlayer magnetism in vdW layered magnets results in rich physical properties, including novel layered-dependent magneto-optical effects[1,2], electric-field induced Kerr rotation[7,8], and giant second-order harmonic generation[10].

The long-range FM order can break the time-reversal symmetry, resulting in magneto-optical Kerr and Faraday effects. The Kerr effect was the one used for detecting the spontaneous magnetization of monolayer CrI_3 and few-layer $Cr_2Ge_2Te_6$ in experiments by magneto-optical Kerr effect microscopy[1,2]. The Kerr and Faraday rotation angles are closely related to the spin-dependent off-diagonal terms in the polarizability tensor (or dielectric tensor) relative to the spin-independent diagonal terms[1,11,12]. Such a spin-dependent polarizability tensor can be obtained via first-principles density functional theory (DFT) calculations by considering the spin-orbit coupling (SOC) effect in the magnetic materials as demonstrated in several prior theoretical works[13–15]. However, when the total magnetization of the system (e.g., bilayer CrI_3) is zero due to the interlayer AFM order, Kerr and Faraday rotations vanish since the off-diagonal terms in the polarizability tensor become zero[1]. This calls for another technique to probe the AFM state more effectively.

The magneto-Raman effect has been recently demonstrated to provide such a technique for studying both the FM and AFM orders in 2D magnets[16–19]. Raman intensity of a phonon mode is determined by its Raman tensor, which corresponds to the derivative of the polarizability tensor with respect to the phonon mode's vibration[20–22]. Since the polarizability tensor has spin-dependent anti-symmetric off-diagonal terms[1,11,12], the Raman tensor has spin-dependent off-diagonal terms as well[9,23–26]. More importantly, a system only has one polarizability tensor, but can possess many Raman tensors depending on the number of phonon modes in the system. Therefore, unlike the polarizability tensor, the spin-dependent off-diagonal terms in Raman tensors do not simply vanish when the total magnetization is zero, as Raman tensors of some phonon modes retain the anti-symmetric off-diagonal terms in the AFM state. This allows magneto-Raman spectroscopy to probe both the FM and AFM orders in 2D materials, as recently demonstrated by several experimental works on CrI_3 and VI_3[9,23–26]. Furthermore, the magneto-Raman effect naturally captures the intricate spin-phonon coupling[27]. Finally, compared to scanning magneto-optical Kerr effect microscopy and spin-polarized scanning tunneling

[1]College of Sciences, Northeastern University, Shenyang, 110819, China. [2]Center for Nanophase Materials Sciences, Oak Ridge National Laboratory, Oak Ridge, TN, 37831, USA. ✉e-mail: kongxiangru@mail.neu.edu.cn; liangl1@ornl.gov

microscopy, magneto-Raman spectroscopy is fast, nondestructive, and relatively cheap. Considering the significance of magneto-Raman scattering, it is imperative to develop first-principles simulation capability (i.e., digital twin of magneto-Raman spectroscopy) and a corresponding analytical model that can reveal the underlying mechanism. Although first-principles calculations of magneto-Raman scattering were attempted for monolayer and bulk CrI_3[28,29], it has not yet been demonstrated for bilayer and few-layer CrI_3 (the focus of most experimental works), let alone other 2D magnets. In addition, to the best of our knowledge, no generalized model derived from the theory of Raman scattering has been developed.

In this work, we have carried out systematic investigations of the magneto-Raman effect in CrI_3 from single-layer (1L) to four-layer (4L) by performing first-principles simulations and developing a generalized polarizability model that can be broadly applied to 2D magnets of any thickness. The calculated polarized Raman spectra of 1L CrI_3 with intralayer FM order and 2L-4L CrI_3 with both interlayer FM and AFM orders agree well with existing experimental data[9,23–25], capturing how Raman selection rules are changed due to the magnetic order, including Raman activation of odd-parity phonon modes. The model successfully reveals how the change of spin orientation in each layer is coupled to the layer's vibration pattern to induce or eliminate the anti-symmetric off-diagonal terms in the Raman tensor and subsequently to alter the Raman intensity of a phonon mode. In addition, our simulations and modeling demonstrate that a similar magneto-Raman effect should be present in $MnBi_2Te_4$, a novel 2D topological magnetic material[30–32], but it has not yet been experimentally observed. The quantitative analysis provided by DFT calculations sheds light on the underlying reason and reveals how to observe it experimentally. Furthermore, we show that the magneto-Raman effect exists in $CrCl_3$ as well, but the change of the magnetic order from the out-of-plane to in-plane direction alters the location of the anti-symmetric off-diagonal terms in the Raman tensor and thus the Raman optical selection rules. Finally, to the best of our knowledge, our work uncovers the spin dependence of E modes for the first time in 2D magnets and predicts how they can be studied experimentally. We demonstrate that the correlation between phonon modes and magnetic orders is much more broadly present than the sole A^2 mode of CrI_3 studied in experiments.

Results

Theory of resonant and magneto-Raman scattering

Raman intensity of a phonon mode j can be expressed as $I \propto \frac{n_j+1}{\omega_j}|\mathbf{e}_s \cdot \mathbf{R} \cdot \mathbf{e}_i^T|^2$, where $\mathbf{e}_s$ and $\mathbf{e}_i$ are the electric polarization vectors of the scattered and incident light, respectively, and $\mathbf{R}$ is the Raman tensor associated with the phonon mode. ω_j is the frequency of the phonon mode j, and $n_j = (e^{\hbar\omega_j/k_BT}-1)^{-1}$ is the Boltzmann distribution function at the given temperature T. According to the Placzek approximation[20–22,33,34], the matrix element of the 3×3 Raman tensor of the phonon mode j is given by

$$R_{\alpha\beta}(j) = V\sum_{\mu=1}^{N}\sum_{l=1}^{3}\frac{\partial\chi_{\alpha\beta}}{\partial r_l(\mu)}\frac{e_l^j(\mu)}{\sqrt{M_\mu}} \quad (1)$$

in which V is the volume of the primitive cell, $\chi_{\alpha\beta}$ is the electric polarizability tensor, $r_l(\mu)$ is the position along the l direction of the μ-th atom ($l = x$, y, or z), $\frac{\partial\chi_{\alpha\beta}}{\partial r_l(\mu)}$ is the derivative of the polarizability tensor over the atomic displacement along the l direction, $e_l^j(\mu)$ is the atomic displacement along the l direction of the μ-th atom for the jth phonon mode (i.e., the eigenvector of the dynamic matrix), and M_μ is the atomic mass. Basically, one needs to calculate the derivatives of the polarizability tensor with respect to the atomic displacements for obtaining the Raman tensor. For non-resonant Raman scattering, we often ignore the dependence of the polarizability tensor on the incident photon energy and only calculate the static polarizability (or dielectric) constant at the zero photon energy[20,21]. However, to capture the photon energy dependence of Raman intensity in resonant Raman scattering, one needs to compute the frequency-dependent polarizability tensor at different atomic displacements and thus obtain the Raman tensor at the laser excitation energy E_L using the finite difference method[22,33,34]. Here, we computed complex $\chi_{\alpha\beta}(E_L)$ for each atomic displacement using the independent particle approximation, where the imaginary part is determined by a summation over all valence/conduction bands at every k-point in the Brillouin zone that satisfies the energy conservation, and the real part is obtained by the usual Kramers-Kronig transformation[35]. Finally, the derivatives of the polarizability tensor, combined with the phonon frequencies and phonon eigenvectors, yield the Raman tensor matrix and, subsequently, the Raman intensity for every phonon mode under a given laser polarization set-up. In the common experimental back-scattering geometry (light z in and z out), the polarization vectors of the scattered and incident light are in-plane (i.e., x–y). The Raman intensity can be simplified when the polarizations are along the crystalline axes (denoted as XX, XY, YY, YZ, etc.): $I(XX) \propto |R_{11}|^2$ when $\mathbf{e}_s = \mathbf{e}_i = (1, 0, 0)$; $I(XY) \propto |R_{12}|^2$ when $\mathbf{e}_s = (1, 0, 0)$, $\mathbf{e}_i = (0, 1, 0)$; $I(YY) \propto |R_{22}|^2$ when $\mathbf{e}_s = \mathbf{e}_i = (0, 1, 0)$; $I(YZ) \propto |R_{23}|^2$ when $\mathbf{e}_s = (0, 1, 0)$, $\mathbf{e}_i = (0, 0, 1)$.

The general form of the Raman tensor is given by

$$\mathbf{R} = \begin{pmatrix} R_{11} & R_{12} & R_{13} \\ R_{21} & R_{22} & R_{23} \\ R_{31} & R_{32} & R_{33} \end{pmatrix}, \quad (2)$$

where the values of Raman tensor elements are complex and depend on the laser excitation energy[36,37], which can be numerically computed by the first-principles DFT method outlined above. If the time-reversal symmetry is preserved in the system, the Raman tensor is symmetric, i.e., $R_{ij} = R_{ji}$. However, for electronic and vibrational Raman scattering of a magnetic material, the Raman tensor can be much more complicated since the magnetic order can break the time-reversal symmetry of the system[9,23–26,28,29]. It can be composed of a symmetric (S) spin-independent part ($\mathbf{R^S}$) where $R_{ij}^S = R_{ji}^S$ and an anti-symmetric (AS) spin-dependent part ($\mathbf{R^{AS}}$) where $R_{ij}^{AS} = -R_{ji}^{AS}$. In other words, $\mathbf{R} = \mathbf{R^S} + \mathbf{R^{AS}}$, where

$$\mathbf{R^S} = \begin{pmatrix} R_{11}^S & R_{12}^S & R_{13}^S \\ R_{12}^S & R_{22}^S & R_{23}^S \\ R_{13}^S & R_{23}^S & R_{33}^S \end{pmatrix},$$

$$\mathbf{R^{AS}} = \begin{pmatrix} 0 & R_{12}^{AS} & R_{13}^{AS} \\ -R_{12}^{AS} & 0 & R_{23}^{AS} \\ -R_{13}^{AS} & -R_{23}^{AS} & 0 \end{pmatrix}.$$

With $\mathbf{R}$ directly calculated from DFT, the elements in $\mathbf{R^S}$ and $\mathbf{R^{AS}}$ can be subsequently obtained since $R_{ij}^S = (R_{ij} + R_{ji})/2$ and $R_{ij}^{AS} = (R_{ij} - R_{ji})/2$. It is important to note that the SOC effect with the noncollinear magnetic order has to be turned on during the calculations of the polarizability tensor corresponding to each atomic displacement, in order to fully capture the effects of magnetism on the polarizability tensor, the Raman tensor, and subsequently the Raman intensity[28,29]. In other words, the anti-symmetric spin-dependent terms in $\mathbf{R^{AS}}$ require the inclusion of the SOC effect.

Magneto-Raman effect in CrI_3

Monolayer CrI_3 has a space group of $P\bar{3}$ (No. 143), and its unit cell has eight atoms and, thus, 24 normal phonon modes at the Γ point. They are decomposed as $\Gamma_{P\bar{3}} = 8A + 16E$, where the non-degenerate A symmetry modes and two-fold degenerate E symmetry modes are Raman active. As the A modes exhibit strong Raman signals in experiments[9,23–25], we will focus on the analysis of these modes. In particular, the A mode around 127.4 cm^{-1} appears as the strongest Raman peak in experiments, which corresponds to the phonon mode at 124.7 cm^{-1} in our calculations, as shown in Fig. 1. If we do not consider the magnetic order, the point group of $P\bar{3}$ is C_3 and the Raman tensor of an A mode assumes the form on the left side of Eq. (3),

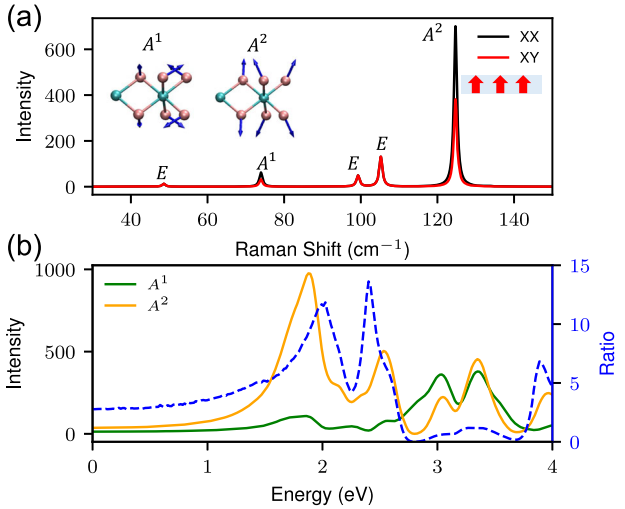

Fig. 1 | Raman spectra of monolayer CrI_3. a Calculated Raman spectra of monolayer CrI_3 under both parallel (XX) and cross (XY) polarizations. The vibration patterns of the two *A* modes are shown as insets. The red arrows indicate the out-of-plane FM order. **b** Calculated resonant Raman intensity versus the photon energy for A^1 (green) and A^2 (orange) modes. The intensity ratio between A^2 and A^1 is shown on the right (blue). Note that the photon energy has been scaled by a factor of 1.63.

where the off-diagonal elements are absent.

$$\mathbf{R}_{\mathrm{no-SOC}} = \begin{pmatrix} a & & \\ & a & \\ & & b \end{pmatrix}, \mathbf{R}_{\mathrm{SOC}} = \begin{pmatrix} a & c & \\ -c & a & \\ & & b \end{pmatrix}. \quad (3)$$

As mentioned above, the inclusion of the magnetic order (either collinear or noncollinear) but without considering the SOC effect does not yield the spin-dependent off-diagonal terms in the Raman tensor. Only after considering the SOC effect[28,29], the Raman tensor develops into a spin-dependent anti-symmetric form, as shown on the right side of Eq. (3). The corresponding calculated values of the Raman tensors are listed in Supplementary Table 1. According to ref. 9, the spin-independent part $\mathbf{R_S}$ is invariant under time-reversal symmetry and independent of the magnetic structure, while the spin-dependent part $\mathbf{R}_{\mathrm{AS}}$ is odd under time-reversal symmetry. This indicates that the reversal of the magnetization direction should change the sign of the anti-symmetric off-diagonal terms in the Raman tensor (i.e., *c* changed to $-c$ while $-c$ changed to *c* in Eq. (3)), which is confirmed by our calculations in Supplementary Table 1. In a first-order approximation, one can say that the anti-symmetric off-diagonal terms are proportional to the magnetization of the system or the applied magnetic field[24,26]. This can also explain why the sign is changed upon the reversal of the magnetization direction of the magnetic field[24,26]. The anti-symmetric Raman tensors in FM monolayer CrI_3 are important for the analysis of Raman tensors and Raman intensities in the few-layer CrI_3 below.

Figure 1a shows the calculated Raman spectra of monolayer CrI_3 in both parallel (XX) and cross (XY) polarization channels. According to prior experimental results and hybrid DFT (HSE06) calculations, monolayer CrI_3's band gap is around 1.52 eV, while bulk CrI_3 has a band gap of about 1.24 eV[38–40]. Our conventional DFT calculations, with the SOC effect included, found the band gap as 0.79 eV for 1L and 0.71 eV for bulk CrI_3. Since DFT underestimates the band gap, the theoretical laser excitation energy is lower than the experimental one, and thus a scaling factor is required to make calculated Raman results more comparable with experiments. By matching calculated Raman spectra of 1L CrI_3 with experimental data produced by a laser line of 1.96 eV[9], we determined the scaling factor as 1.63 and thus the DFT laser excitation energy as 1.20 eV. Although hybrid functional methods such as HSE06 yield better descriptions of the electronic properties of CrI_3, it is computationally prohibitive to use HSE06 for magneto-Raman simulations with noncollinear magnetism and SOC considered. Conventional DFT calculations with a scaling factor provide a balanced approach for satisfactory simulations of magneto-Raman spectra, as will be discussed below. In Fig. 1a, besides the strong peak (A^2) at 124.7 cm^{-1}, there is another mode A^1 at 73.9 cm^{-1} [24] with much weaker intensity (see Supplementary Table 2 for the Raman tensor). Most experimental works focused on A^2 mode due to its stronger signal, but we found out that their intensities can be comparable at certain laser energies. Figure 1b shows the Raman intensities of both modes as a function of the photon energy, called Raman excitation profiles (REPs). At the lower energy window, A^2 shows a stronger Raman resonance effect than A^1. The Raman intensity of A^2 reaches a peak near 2 eV, which is an order of magnitude stronger than that of A^1. With the energy further increasing, the intensity of A^2 begins to decrease, but it is still favorable for experiments to observe (such as the commonly used 1.96 and 2.33 eV laser lines). Starting around 2.5 eV, however, the signal of A^2 decreases, while the intensity of A^1 begins to substantially increase and grows even to be larger than that of A^2 starting from 2.7 eV. At excitation energy at 3 eV, for example, A^1 shows stronger signals than A^2. This is confirmed by the calculated Raman spectra shown in Supplementary Fig. 1. The calculated REPs in Fig. 1b reveal two key findings: first, A^1 can be effectively observed by using a laser line with energy higher than 2.7 eV, but the two most commonly used laser energies are 1.96 and 2.33 eV that often miss this mode; second, the exciton-phonon couplings for A^1 and A^2 have both similarities and differences that arise from their vibration patterns as illustrated in the insets in Fig. 1a. A^2 has atomic vibrations predominantly out-of-plane, while A^1 has both out-of-plane and in-plane vibration components. When an exciton has the wavefunction pointed out-of-plane, it should couple more strongly with A^2, such as at energies between 1.9 and 2.5 eV in Fig. 1b; when an exciton has the wavefunction spreading along both out-of-plane and in-plane directions, it could couple with both A^2 and A^1 so that they share a similar resonance window, e.g., between 3 and 3.5 eV. Such vibration-dependent exciton-phonon coupling behaviors have been previously reported for MoS_2[41] and black phosphorus[42,43].

Because both A^1 and A^2 have out-of-plane components in the vibration patterns, they exhibit strong spin-dependent Raman scattering as their out-of-plane vibration components are coupled with the out-of-plane magnetic order in CrI_3. As shown in Eq. (3), above the Curie temperature where the magnetic order disappears, off-diagonal terms $R_{12} = R_{21} = 0$, and thus *A* symmetry Raman peaks disappear in the cross (XY) polarization since $I(\mathrm{XY}) \propto |R_{12}|^2$[29]. However, below the Curie temperature where the monolayer has an FM order, off-diagonal terms are no longer zero ($R_{12} = -R_{21} = c$), and hence A^1 and A^2 are still present in the XY polarization, although the intensity is weaker than that from the parallel (XX) polarization since $|R_{12}|^2 < |R_{11}|^2$ (Fig. 1a). The appearance of a *A* symmetry Raman peak in the cross-polarization is an important sign that the Raman mode is spin-dependent. Note that A^1 mode is very weak in the XY polarization when the excitation energy is 1.96 or 2.33 eV, since it is already weak in the XX polarization. This explains why A^1 in the XY polarization cannot be differentiated from the background noise and ignored for the magneto-Raman study[9]. However, as discussed above, with a higher excitation energy above 2.7 eV, A^1 is significantly enhanced in both XX and XY polarizations and it shows strong spin dependence just like A^2 (see Supplementary Fig. 1).

As for doubly degenerated *E* modes, the Raman intensity is basically the same for cross and parallel polarization setups (Fig. 1a), a common behavior for 2D materials in hexagonal lattices[21]. This may lead to a partially incorrect conclusion that *E* modes are not correlated with the magnetic order. In fact, we discover that their Raman tensors also have spin-dependent anti-symmetric off-diagonal terms, which correspond to R_{13} and R_{23} instead of R_{12}. In particular, for the characteristic *E* modes at 105.2 cm^{-1}, one of the *E* modes (E^1) has large R_{13}^{AS} while the other (E^2) has large R_{23}^{AS} (see Supplementary Tables 3 and 4, respectively). In the typical back-scattering geometry, R_{13} and R_{23} are not probed by Raman scattering, and thus, their spin-dependent behaviors are completely missed. To study the magneto-Raman scattering of *E* modes, therefore, it is important to change the travel

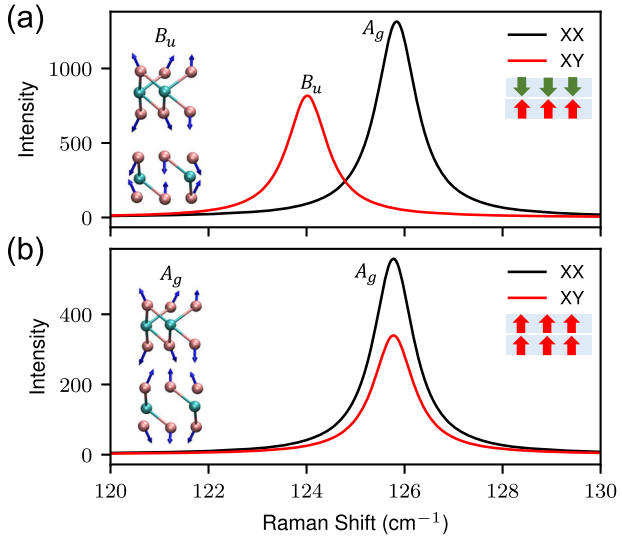

Fig. 2 | Raman spectra of bilayer CrI_3. Calculated Raman spectra of bilayer CrI_3 under both parallel (XX) and cross (XY) polarizations when the interlayer magnetic order is **a** AFM or **b** FM. The vibration patterns of A_g and its Davydov-split counterpart B_u are shown as insets. The red and green arrows indicate the out-of-plane magnetic order.

direction of laser light to the x or y direction so the polarizations of light have z components for effectively capturing the spin-dependent R_{13} and R_{23} of E modes. To the best of our knowledge, our calculations uncover the spin dependence of E modes for the first time in CrI_3 and predict how they can be studied experimentally. These results demonstrate that the correlation between phonon modes and magnetic orders is much more broadly present than the sole A^2 mode studied in experiments.

Bilayer CrI_3 has Davydov splitting of each phonon mode from the monolayer due to the vdW interactions between the layers. For instance, mode A in the monolayer is split into two modes: even-parity mode A_g and odd-parity mode B_u. A simple linear chain model can explain the Davydov splitting[23]. As shown in the insets in Fig. 2, A_g mode vibrates in phase between layers while B_u mode vibrates out of phase between layers. Without a magnetic order, the crystallographic space group of the bilayer belongs to $C2/m$ (No. 12), and the point group is $C_{2h}(2/m)$. A_g is Raman active with a symmetric form of Raman tensor. However, with the inclusion of the magnetic order and SOC, it becomes much more complicated with anti-symmetric off-diagonal terms. In addition, the Raman inactive mode B_u also becomes active under the interlayer AFM order and shows up under the cross-polarization setup, as shown in Fig. 2. Note that the irreducible representations of phonon modes, such as A_g and B_u, originate from the crystallographic space group and strictly speaking should change with the magnetic order to reflect the change in the Raman tensors. However, for simplicity and consistency, we keep using the same symmetry notations for phonon modes regardless of the magnetism. Our first-principles simulated Raman spectra are well consistent with prior experimental results[9,23–25]. More importantly, our numerical simulations provide an atomic scale picture of the spin-phonon coupling and reveal how a magnetic order can introduce the anti-symmetric Raman tensor elements, which enables us to propose a unified model to explain the spin dependence of Raman modes in 2D magnets.

Since the interlayer coupling in CrI_3 is weak, we can treat each layer approximately as a single object[23,44] and rewrite the Raman tensor in Eq. (1) with each layer instead of each atom as a unit:

$$\mathbf{R} = V\sum_{L=1}^{N}\frac{\partial\chi_{\alpha\beta}}{\partial r_l(L)}\frac{e_l^j(L)}{\sqrt{M_L}} \propto \sum_{L=1}^{N}\frac{\partial\chi_{\alpha\beta}}{\partial d(L)}\Delta d_L \propto \sum\nolimits_{L=1}^{N} P_{\alpha\beta}^{L}\Delta d_L, \quad (4)$$

where L is the layer index, N is the total number of layers, $P_{\alpha\beta}^{L}$ represents the contribution of layer L to the change of polarizability by a unit displacement of the layer, and Δd_L indicates the displacement of layer L in a phonon mode. $P_{\alpha\beta}^{L}$ can also be divided into a symmetric part P_S and an anti-symmetric part P_{AS} since $\chi_{\alpha\beta}$ has both symmetric and anti-symmetric parts. Eq. (4) represents a generalized and simplified polarizability model for us to gain crucial insights into Raman scattering of 2D magnets, as will be discussed below.

For the bilayer, $\mathbf{R} \propto P^1\Delta d_1 + P^2\Delta d_2$. The symmetric parts of the polarizability tensor of layer 1 and layer 2 are equal regardless of the magnetic order between the layers, i.e., $\chi_S^1 = \chi_S^2 = \chi_S$; however, the anti-symmetric parts depend on the relative spin orientation between the layers. In the AFM state, two layers have the opposite spin alignments, and thus $\chi_{AS}^1 = -\chi_{AS}^2 = \chi_{AS}$ (recall a similar behavior that the reversal of the spin direction in the monolayer changes the sign of the anti-symmetric terms in the Raman tensor); in the FM state, it is natural that $\chi_{AS}^1 = \chi_{AS}^2 = \chi_{AS}$. Therefore $P_S^1 = P_S^2 = P_S, P_{AS}^1 = -P_{AS}^2 = P_{AS}$ for the AFM state and $P_{AS}^1 = P_{AS}^2 = P_{AS}$ for the FM state. For the monolayer, $\mathbf{R} \propto P^1\Delta d_1 = (P_S + P_{AS})\Delta d_1$. Therefore, P_S and P_{AS} essentially correspond to the symmetric and anti-symmetric part of Raman tensor of A^2 mode in monolayer CrI_3, respectively, and they should assume the following simple forms according to Eq. (3):

$$P_S = \begin{pmatrix} a & & \\ & a & \\ & & b \end{pmatrix}, P_{AS} = \begin{pmatrix} & c & \\ -c & & \\ & & \end{pmatrix}. \quad (5)$$

For the AFM state, we have $\mathbf{R} \propto P_S(\Delta d_1 + \Delta d_2) + P_{AS}(\Delta d_1 - \Delta d_2)$. For A_g mode (Fig. 2), $\Delta d_1 \approx \Delta d_2$, and thus $\mathbf{R}_{A_g}^{AFM} \propto 2P_S\Delta d_1$ that only has the symmetric part; for B_u mode, $\Delta d_1 \approx -\Delta d_2$, and thus $\mathbf{R}_{B_u}^{AFM} \propto 2P_{AS}\Delta d_1$ that only has the anti-symmetric part. This analysis is confirmed by the numerical Raman tensors from DFT calculations shown in Supplementary Table 5. Clearly, the Raman tensor of A_g (B_u) mode almost only has diagonal (off-diagonal) terms so that it almost only appears in the XX (XY) polarization set-up, as shown in Fig. 2a. For the FM state, on the other hand, we have $\mathbf{R} \propto (P_S + P_{AS})(\Delta d_1 + \Delta d_2)$. For B_u mode, $\Delta d_1 \approx -\Delta d_2$, so its Raman tensor is basically zero, which is consistent with our DFT calculations shown in Supplementary Table 5. For A_g mode, $\Delta d_1 \approx \Delta d_2$, $\mathbf{R}_{A_g}^{FM} \propto 2(P_S + P_{AS})\Delta d_1$, so the Raman tensor contains both the symmetric P_S and anti-symmetric P_{AS}, indicating a much more complicated form similar to the one on the right side of Eq. (3). As shown in Fig. 2b, we can observe that B_u mode is inactive but A_g mode is active in both polarization setups. These trends are similar to the A^2 mode of the monolayer shown in Fig. 1, since the bilayer here shares the same FM state with the monolayer. To summarize, our model successfully explains the experimental and DFT simulated magneto-Raman behaviors of A_g mode and the Davydov-split component B_u. It also reveals two key ingredients governing the abnormal behaviors of A_g and B_u modes under the AFM order: first, the opposite spin orientation between two layers gives rise to opposite anti-symmetric terms in the polarizability and Raman tensors between two layers; second, A_g and B_u modes have the opposite layer vibration patterns. Therefore, the spin-phonon coupling in CrI_3 depends on both the magnetic order (reflected in P_{AS}) and the vibration pattern (reflected in Δd_L).

Trilayer CrI_3 has three Davydov splitting components for each phonon mode from the monolayer. For A^2 mode in monolayer, it is split into three modes: two even-parity modes A_g and one odd-parity mode B_u, as shown in Fig. 3a. Their simulated Raman spectra exhibit strong dependence on the interlayer magnetic order as demonstrated in Fig. 3b, c, in agreement with the prior experimental work[23]. We continue to deploy our model for understanding both the experimental and our calculated magneto-Raman spectra. The Raman tensor of the trilayer can be written as $\mathbf{R} \propto P^1\Delta d_1 + P^2\Delta d_2 + P^3\Delta d_3$. In the AFM state, the polarizability tensor of each layer follows $\chi_S^1 = \chi_S^2 = \chi_S^3 = \chi_S$, $\chi_{AS}^1 = -\chi_{AS}^2 = \chi_{AS}^3 = \chi_{AS}$. Therefore $P_S^1 = P_S^2 = P_S^3 = P_S$, $P_{AS}^1 = -P_{AS}^2 = P_{AS}^3 = P_{AS}$, leading to $\mathbf{R} \propto P_S(\Delta d_1 + \Delta d_2 + \Delta d_3) + P_{AS}(\Delta d_1 - \Delta d_2 + \Delta d_3)$. For B_u mode, $\Delta d_2 = 0$, and $\Delta d_1 \approx -\Delta d_3$, so $\mathbf{R}$ is essentially zero and B_u mode does not become active in the AFM order. However, for A_g^1 mode, $\Delta d_1 \approx \Delta d_3 = \Delta d$, while $\Delta d_2 = -\Delta d'$ which is in the opposite direction but larger than Δd. This yields

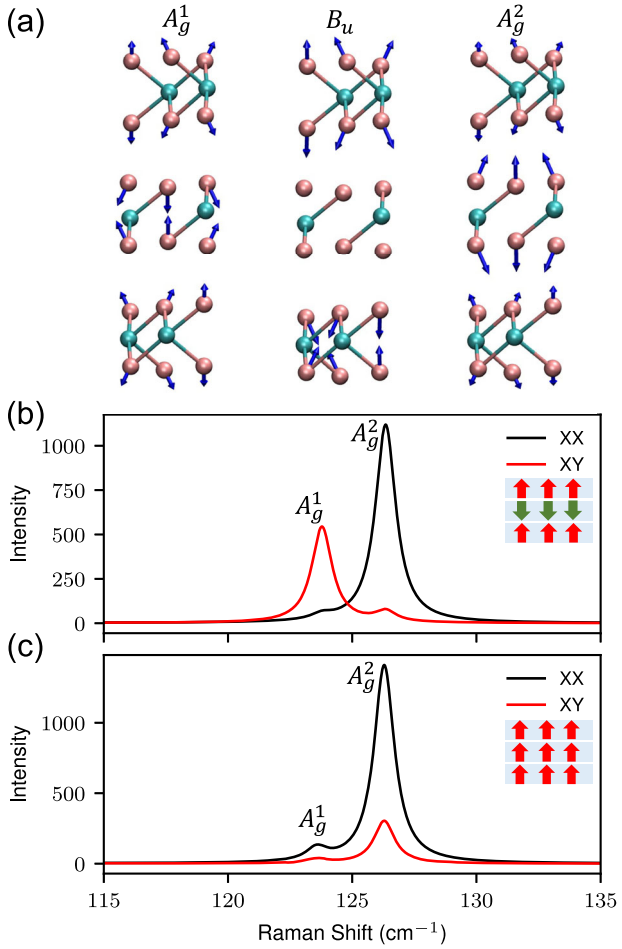

Fig. 3 | Vibration patterns and Raman spectra of trilayer CrI_3. a The vibration patterns of three Davydov splitting components for the Raman mode around 125 cm^{-1} in trilayer CrI_3. Calculated Raman spectra of trilayer CrI_3 under both parallel (XX) and cross (XY) polarizations when the interlayer magnetic order is **b** AFM or **c** FM.

$\mathbf{R}_{A_g^1}^{\mathrm{AFM}} \propto P_S(2\Delta d - \Delta d') + P_{AS}(2\Delta d + \Delta d')$, where $2\Delta d - \Delta d'$ is smaller than $2\Delta d + \Delta d'$. Recall Eq. (5), and we can conclude that the diagonal terms in the Raman tensor of A_g^1 are smaller than the off-diagonal anti-symmetric terms. Therefore, A_g^1 exhibits stronger signals in the XY polarization setup than that in the XX polarization setup as demonstrated in Fig. 3b. On the other hand, for A_g^2 mode, $\Delta d_1 \approx \Delta d_3 = \Delta d''$, while $\Delta d_2 = \Delta d'''$ that is in the same direction as Δd_1 and Δd_3, leading to $\mathbf{R}_{A_g^2}^{\mathrm{AFM}} \propto P_S(2\Delta d'' + \Delta d''') + P_{AS}(2\Delta d'' - \Delta d''')$. It is apparent that the diagonal terms in the Raman tensor of A_g^2 should be larger, and hence it shows stronger signals in Fig. 3b in the parallel polarization setup than that in the cross-polarization setup, which is the opposite behavior of A_g^1.

In the FM state, the Raman tensor is rewritten as $\mathbf{R} \propto P_S(\Delta d_1 + \Delta d_2 + \Delta d_3) + P_{AS}(\Delta d_1 + \Delta d_2 + \Delta d_3)$. B_u mode still has its Raman tensor as zero and is Raman inactive. For A_g^1 mode, $\Delta d_1 \approx \Delta d_3 = \Delta d$, $\Delta d_2 = -\Delta d'$, and thus $\mathbf{R}_{A_g^1}^{\mathrm{FM}} \propto (P_S + P_{AS})(2\Delta d - \Delta d')$. As $2\Delta d - \Delta d'$ is very small, the Raman intensity of A_g^1 is weak in both polarization channels, as shown in Fig. 3c. For A_g^2 mode, $\mathbf{R}_{A_g^2}^{\mathrm{FM}} \propto (P_S + P_{AS})(2\Delta d'' + \Delta d''')$. This suggests that A_g^2 should be stronger in both polarization channels compared to A_g^1 since $2\Delta d'' + \Delta d'''$ is much larger than $2\Delta d - \Delta d'$, as confirmed by calculated Raman spectra in Fig. 3c. Moreover, the Raman tensor of A_g^2 assumes a similar form to that of A^2 mode in monolayer CrI_3, since the latter is $\mathbf{R} \propto (P_S + P_{AS})\Delta d_1$ for the monolayer. Therefore, similar to A^2 mode shown in Fig. 1a, the Raman intensity of A_g^2 in the XX channel is stronger than that in the XY channel. Raman intensities of the relevant phonon modes in 1L-3L CrI_3 based on the generalized polarizability model are summarized below (more details in Supplementary Information):

$$
\begin{gathered}
\text{1L}: \\
I_{A^2}(\mathrm{XX}) \propto |R_{11}|^2 = |a|^2\Delta d_1^2, \quad I_{A^2}(\mathrm{XY}) \propto |R_{12}|^2 = |c|^2\Delta d_1^2; \\
\text{2L}: \\
I_{A_g}^{\mathrm{AFM}}(XX) \propto 4|a|^2\Delta d_1^2, \qquad I_{A_g}^{\mathrm{AFM}}(XY) = 0, \\
I_{B_u}^{\mathrm{AFM}}(XX) = 0, \; I_{B_u}^{\mathrm{AFM}}(XY) \propto 4|c|^2\Delta d_1^2, \\
I_{A_g}^{\mathrm{FM}}(XX) \propto 4|a|^2\Delta d_1^2, \; I_{A_g}^{\mathrm{FM}}(XY) \propto 4|c|^2\Delta d_1^2, \\
I_{B_u}^{\mathrm{FM}}(XX) = 0, \; I_{B_u}^{\mathrm{FM}}(XY) = 0; \\
\text{3L}: \\
I_{A_g^1}^{\mathrm{AFM}}(XX) \propto |a|^2(2\Delta d - \Delta d')^2, I_{A_g^1}^{\mathrm{AFM}}(XY) \propto |c|^2(2\Delta d + \Delta d')^2, \\
I_{B_u}^{\mathrm{AFM}}(XX) = 0, \; I_{B_u}^{\mathrm{AFM}}(XY) = 0, \\
I_{A_g^2}^{\mathrm{AFM}}(XX) \propto |a|^2(2\Delta d'' + \Delta d''')^2, I_{A_g^2}^{\mathrm{AFM}}(XY) \propto |c|^2(2\Delta d'' - \Delta d''')^2, \\
I_{A_g^1}^{\mathrm{FM}}(XX) \propto |a|^2(2\Delta d - \Delta d')^2, \; I_{A_g^1}^{\mathrm{FM}}(XY) \propto |c|^2(2\Delta d - \Delta d')^2, \\
I_{B_u}^{\mathrm{FM}}(XX) = 0, \; I_{B_u}^{\mathrm{FM}}(XY) = 0, \\
I_{A_g^2}^{\mathrm{FM}}(XX) \propto |a|^2(2\Delta d'' + \Delta d''')^2, I_{A_g^2}^{\mathrm{FM}}(XY) \propto |c|^2(2\Delta d'' + \Delta d''')^2,
\end{gathered}
$$

which are consistent with ab initio calculated Raman spectra shown in Figs. 1, 2, 3, respectively. In short, the model can explain the magneto-Raman scattering data in 1L-3L CrI_3, as well as the four-layer and bulk CrI_3 systems (see more details in Supplementary Information and Supplementary Figs. 2, 3). The comparison between Raman spectra from first-principles calculations and the model is shown in Supplementary Fig. 4. Our calculated spin-dependent polarized Raman spectra of 1L-4L CrI_3 are also consistent with existing experimental data (Supplementary Fig. 5). Finally, we note that the circularly polarized magneto-Raman spectra can also be predicted by our DFT simulations and explained by the model (more details in Supplementary Information).

Magneto-Raman effect in $MnBi_2Te_4$

$MnBi_2Te_4$ is another 2D vdW magnetic material that has attracted broad research interests due to its novel topological and magnetic properties[30–32]. The crystal structure of bulk $MnBi_2Te_4$ belongs to the space group $R\bar{3}m$ (No. 166) with the point group D_{3d}, and it has three doubly degenerate E_g Raman modes and three non-degenerate A_{1g} Raman modes[45,46]. Similar to CrI_3, the spin-dependent anti-symmetric off-diagonal matrix elements of $MnBi_2Te_4$ appear in R_{13} and R_{23} for E_g modes, while in R_{12} for A_{1g} modes. Therefore, in the typical back-scattering geometry, only A_{1g} modes can be probed for the spin-Raman correlation (R_{12} for E_g modes is spin-independent). Following the similar steps of bilayer CrI_3 discussed above, we have $\mathbf{R} \propto P_S(\Delta d_1 + \Delta d_2) + P_{AS}(\Delta d_1 - \Delta d_2)$ for the AFM state. For a A_{1g} mode in Fig. 4a (in-phase layer vibrations), $\Delta d_1 \approx \Delta d_2$, and thus $\mathbf{R}_{A_{1g}}^{\mathrm{AFM}} \propto 2P_S\Delta d_1$; for a A_{2u} mode (out-of-phase layer vibrations), $\Delta d_1 \approx -\Delta d_2$, and thus $\mathbf{R}_{A_{2u}}^{\mathrm{AFM}} \propto 2P_{AS}\Delta d_1$. Therefore, the Raman tensor of a A_{1g} (A_{2u}) mode only has diagonal (off-diagonal) terms in the AFM state so that it only appears in the XX (XY) polarization channel, which well explains the spin-dependent behaviors of three A_{1g} and A_{2u} modes in our calculated Raman spectra shown in Fig. 4b. For the FM state, we have $\mathbf{R} \propto (P_S + P_{AS})(\Delta d_1 + \Delta d_2)$. For a A_{2u} mode, $\Delta d_1 \approx -\Delta d_2$, so $\mathbf{R}_{A_{2u}}^{\mathrm{FM}} \approx 0$. For a A_{1g} mode, $\Delta d_1 \approx \Delta d_2$, and thus $\mathbf{R}_{A_{1g}}^{\mathrm{FM}} \propto 2(P_S + P_{AS})\Delta d_1$. These results corroborate our calculations in Fig. 4c that any A_{2u} mode is inactive, but any A_{1g} mode can show up in both linear polarization setups (see circularly polarized Raman spectra of $MnBi_2Te_4$ in Supplementary information). In short, $MnBi_2Te_4$ exhibits a similar magneto-Raman effect to CrI_3. Our first-principles calculations and the generalized model demonstrate that the magneto-Raman scattering of phonon modes should broadly exist in 2D magnets. Finally, we note that compared to CrI_3, the spin-dependent off-diagonal terms in $MnBi_2Te_4$ are obviously smaller (Supplementary Table 7) since the intensities of A_{2u} modes in Fig. 4b and A_{1g} modes in Fig. 4c in the XY channel are in general

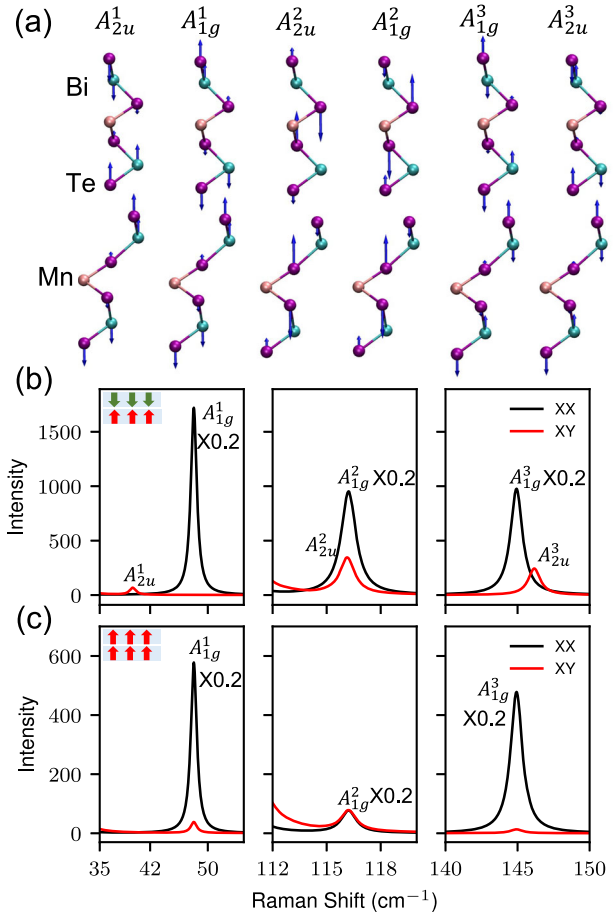

Fig. 4 | Vibration patterns and Raman spectra of bulk $MnBi_2Te_4$. a Calculated vibration patterns of three A_{1g} Raman modes and their Davydov-split counterparts in bulk $MnBi_2Te_4$. Calculated Raman spectra of bulk $MnBi_2Te_4$ under both parallel (XX) and cross (XY) polarizations when the interlayer magnetic order is **b** AFM or **c** FM. The Raman spectra in the XX channel are reduced by five times, so A_{2u} modes in (**b**) and A_{1g} modes in (**c**) from the XY channel are more visible.

considerably weaker than those in the XX channel (even the intensities in XX are reduced by five times). Such a result predicted by the first-principles simulations may explain why the spin-dependent phenomenon of $MnBi_2Te_4$ has not yet been experimentally observed since the spin-related Raman signals could be too weak. Based on our calculations, exploring different laser excitation energies other than 1.96 and 2.33 eV, or applying a strong magnetic field should boost the signals for detection.

We have also studied bilayer $MnBi_2Te_4$ (Fig. 5), where a notable difference from the bulk is the appearance of three additional A_{1g} and A_{2u} Davydov pairs besides the three bulk-like A_{1g} and A_{2u} pairs. This is due to the symmetry reduction in the bilayer as the exterior atoms in each layer are no longer equivalent to the interior atoms. These new Davydov pairs are denoted as A'_{1g} and A'_{2u}, A''_{1g} and A''_{2u}, and A'''_{1g} and A'''_{2u}, respectively, to differentiate the bulk-like pairs (A^1_{1g} and A^1_{2u}, A^2_{1g} and A^2_{2u}, and A^3_{1g} and A^3_{2u}). All six Davydov pairs in 2L $MnBi_2Te_4$ exhibit similar magneto-Raman behaviors to bulk $MnBi_2Te_4$. Just like the bulk, the magneto-Raman effect of most pairs in 2L $MnBi_2Te_4$ is weaker than CrI_3 since the spin-related Raman intensities in the XY channel are generally much weaker than intensities in the XX channel (even the latter are reduced by five times for most Raman peaks). However, it is interesting to note that for the A'_{1g} and A'_{2u} pair that only shows up in 2L $MnBi_2Te_4$, the intensities in the cross channel are stronger than or comparable with those in the parallel channel, indicating a strong magneto-Raman effect. This is probably due to strong displacements of the Mn atoms and the neighboring Te atoms in the vibrations of A'_{1g} and A'_{2u} modes as these atoms host the majority of magnetic moments in the system. For the A'''_{1g} and A'''_{2u} pair involving strong displacements of the Mn atoms, the magneto-Raman effect is also relatively strong compared to many other modes. In short, 2L and few-layer $MnBi_2Te_4$ could present interesting magneto-Raman phenomena for future experimental exploration.

Magneto-Raman effect in $CrCl_3$ with in-plane magnetization

$CrCl_3$ is a 2D layered magnet that features an in-plane easy axis where magnetic orders are within the $x-y$ plane[47–49], compared to CrI_3 and $MnBi_2Te_4$ that have an out-of-plane easy axis. We investigated bilayer $CrCl_3$, where the spins are set along with the x axis without loss of generality. Similar magneto-Raman effect is found for $CrCl_3$ (Supplementary Fig. 8); however, there are two notable differences between $CrCl_3$ and CrI_3. First, due to the in-plane magnetic orders, the major spin-dependent anti-symmetric terms in Raman tensors of A_g and B_u modes appear in R_{23} and R_{32} for $CrCl_3$ (Supplementary Table 6) compared to R_{12} and R_{21} for CrI_3 (Supplementary Table 5). Therefore, the magneto-Raman phenomena of $CrCl_3$ are better observed when the travel direction of light is along the x axis (i.e., the laser geometry should be $\bar{X}(YY)X$ or $\bar{X}(YZ)X$ instead of the common back-scattering $\bar{Z}(XX)Z$ or $\bar{Z}(XY)Z$, see Supplementary Fig. 8). Second, because of its weaker SOC[29,50], the spin-dependent off-diagonal terms in Raman tensors of $CrCl_3$ are significantly smaller than the diagonal terms and hence the intensities in the cross channel are much weaker than those in the parallel channel (Supplementary Fig. 8), in contrast to CrI_3 where the intensities in both the channels are comparable (Fig. 2). The comparative study between $CrCl_3$ and CrI_3 highlights that the spin orientation and the SOC strength are both crucial in governing magneto-Raman behaviors.

Finally, to demonstrate the robustness of our results, we tested different functionals (LDA and PBE) and vdW correction models (semi-empirical D3 corrections and non-local vdW-DF functional optB86b-vdW) on 2L CrI_3 and 2L $MnBi_2Te_4$. These different calculation methods give rise to minor differences in the spin-dependent polarized Raman spectra while the magneto-Raman behaviors and the optical selection rules remain the same (Supplementary Figs. 9, 10), proving the validity of our magneto-Raman findings.

Discussion

In summary, we have carried out a comprehensive study of the magneto-Raman effect in 2D magnets by using first-principles DFT calculations and a simple yet generalized polarizability model derived from the theory of Raman scattering. For 1L CrI_3, the out-of-plane FM magnetic order is found to introduce considerable anti-symmetric off-diagonal terms in the Raman tensor of the characteristic A symmetry mode near 125 cm^{-1} (denoted as A^2 or A_g), which alters its optical selection rule so that it can be observed in the cross (XY) polarization channel. Such strong spin-phonon coupling also gives rise to a notable degree of circular polarization (i.e., Raman intensity is different in LL and RR circular polarization channels). Without the FM order, our simulations prove that such a magneto-Raman effect is completely absent. Our results are well consistent with prior experimental works, and more importantly, we discover that such spin-dependent off-diagonal terms are also present for another A symmetry mode near 74 cm^{-1} and several doubly degenerated E modes in 1L CrI_3. DFT calculations provide quantitative evidence on why they are almost not studied and predict how they can be experimentally observed. This demonstrates that the correlation between phonon modes and magnetic orders is not limited to the sole A symmetry Raman mode studied in experiments so far, and it should be a universal phenomenon.

For 2L-4L CrI_3, the calculated linearly and circularly polarized Raman spectra for both interlayer FM and AFM orders also agree well with the experimental data, highlighting the strong magnetism dependence of the Davydov-split components of A_g mode. The normally Raman inactive Davydov modes with B_u symmetry remain silent under the FM state, but can become Raman active under the AFM state as the anti-symmetric off-diagonal terms appear in the Raman tensor; the Davydov modes with A_g symmetry have anti-symmetric off-diagonal terms under the FM state, but can have these terms disappear under the AFM state. Such spin-dependent

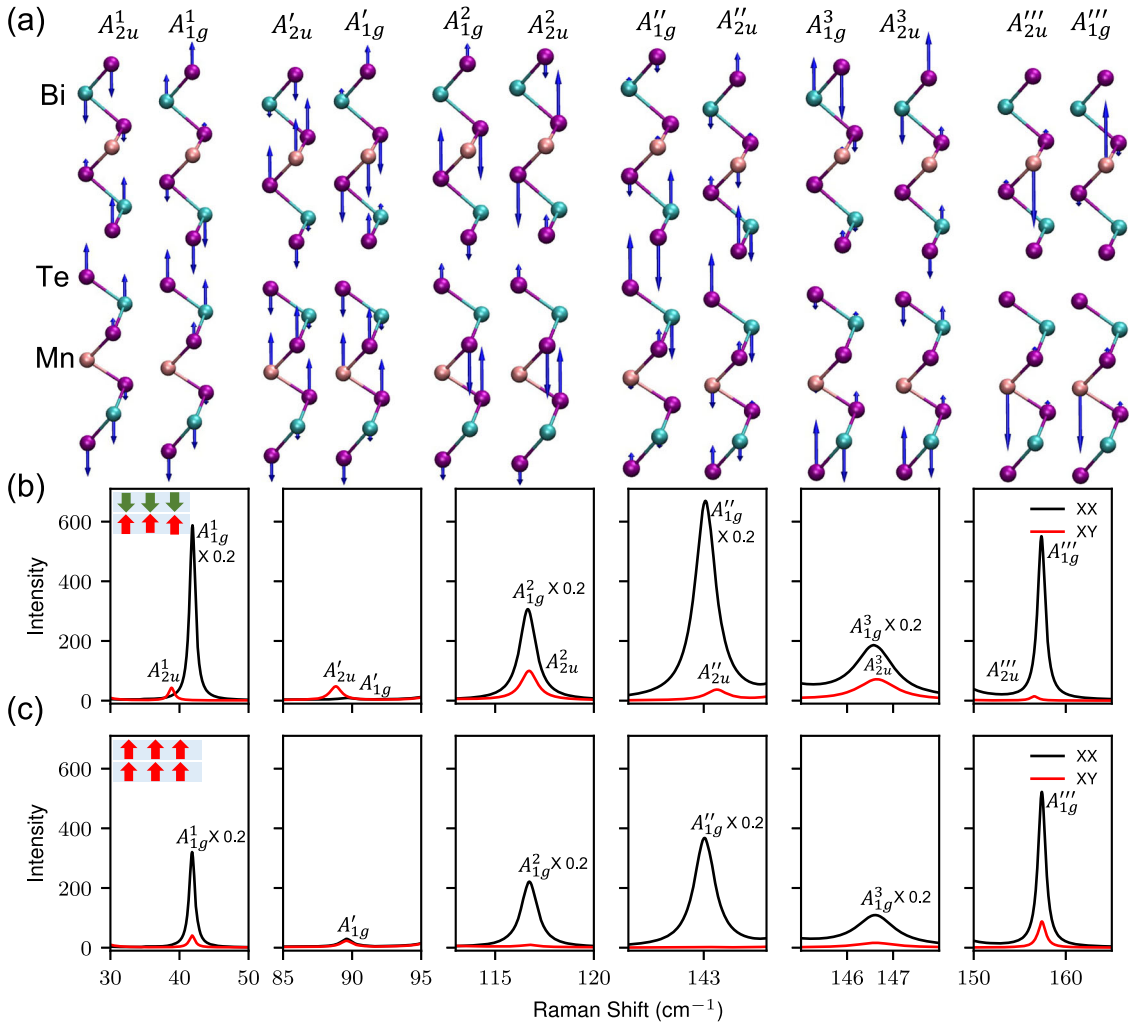

Fig. 5 | Vibration patterns and Raman spectra of bilayer $MnBi_2Te_4$. a Calculated vibration patterns of six A_{1g} and A_{2u} Davydov pairs in 2L $MnBi_2Te_4$. Calculated Raman spectra of 2L $MnBi_2Te_4$ under both parallel (XX) and cross (XY) polarizations when the interlayer magnetic order is **b** AFM or **c** FM. The intensities of four Raman peaks in the XX channel are reduced by five times so Raman peaks from the XY channel are more visible.

behaviors change the selection rules for both linear and circular polarizations and allow magneto-Raman spectroscopy to monitor the magnetic order. Our generalized polarizability model successfully explains the magneto-Raman spectra of 2L-4L CrI_3 and can be applied to any thickness in principles. It reveals that the spin-phonon coupling in 2D magnets depends on both the spin orientation (reflected in P_{AS}) and the vibration pattern (reflected in Δd_L) of each layer. Furthermore, we extend our simulations and modeling to $MnBi_2Te_4$ and reveal a similar magneto-Raman effect. The quantitative results by DFT calculations unveil why it has not yet been observed experimentally and present a path forward on how we can observe it in future experiments. Finally, we investigated 2L $CrCl_3$ that has an in-plane easy axis, in contrast to CrI_3 and $MnBi_2Te_4$ that have an out-of-plane easy axis. Although the magneto-Raman effect is still present, the in-plane magnetic order in $CrCl_3$ changes the location of the major spin-dependent off-diagonal terms in the Raman tensor matrix, leading to different polarization selection rules. The weak SOC in $CrCl_3$ renders its magneto-Raman effect much weaker than CrI_3, and thus selecting different laser excitation energies and applying a strong magnetic field may be required for experimental detection.

Our first-principles simulations and analytical modeling are complementary to each other in a sense that the former provides quantitative Raman spectra guiding experiments to locate phonon modes showing magneto-Raman behaviors and the latter offers qualitative analysis facilitating the understanding of the phenomena. They could play an important role in accelerating the magneto-Raman research in the ever-growing family of 2D magnets. With the prediction power of first-principles simulations, in the future, we will generate a computational magneto-Raman library (i.e., digital twin of magneto-Raman spectroscopy) to facilitate rapid characterization of magnetic ordering in layered 2D magnets.

Methods

DFT parameters

First-principles spin-polarized DFT calculations are carried out using the Vienna ab initio simulation package (VASP) with the projected augmented wave (PAW) method[51,52]. Local density approximation (LDA) is adopted for the electron exchange-correlation functional for CrI_3, since the phonon frequencies computed by LDA are well consistent with experimental data. The generalized gradient approximation (GGA) of Perdew, Burke, and Ernzerhof (PBE)[53] is also used for the exchange-correlation functional, where both the DFT-D3 method[54] (denoted as PBE + D3) and the optB86b-vdW functional[55] (denoted as PBE + optB86b) are added to describe the van der Waals (vdW) interactions between the layers. The PBE + D3 and PBE + optB86b, however, notably underestimate the phonon frequencies of CrI_3, and thus LDA is used for phonon and Raman intensity calculations of CrI_3. On the other hand, PBE+D3 describes the lattice dynamics of $MnBi_2Te_4$ reasonably well[46], and hence it is used for computing properties of

$MnBi_2Te_4$. To account for the strong electron correlations effect from the localized *d* orbitals of Cr and Mn atoms, we employ Dudarev's DFT + *U* approach[56], where the effective *U* term is $U_{eff} = 3.0$ eV for CrI_3[5] while 4.0 eV for $MnBi_2Te_4$[30]. For both CrI_3 and $MnBi_2Te_4$, each layer prefers the FM order with an out-of-plane easy axis[1,30]. The weak interlayer interactions, however, make it possible to switch interlayer magnetism between the FM and AFM order[9,23–26]. Therefore, we consider both interlayer AFM and FM magnetic orders in our calculations. All the structures are relaxed until the maximum force on each atom is less than 1 meV/Å. The cutoff energy of the plane waves is chosen as 350 eV. The Brillouin zone (BZ) is sampled using Γ-centered $12 \times 12 \times 1$ for mono- and few-layer CrI_3 and bilayer $MnBi_2Te_4$, while $12 \times 12 \times 3$ uniform k-grid for bulk CrI_3 and $MnBi_2Te_4$. For the 2D systems, a vacuum region of more than 20 Å in the direction is used to avoid spurious interactions with the neighboring cells. We also studied bilayer $CrCl_3$ using the same setting as bilayer CrI_3 with the PBE+D3 method; however, the magnetic orders (both FM and AFM) were set in-plane for $CrCl_3$.

Phonon calculations

Based on the optimized unit cell, we perform phonon calculations using a finite difference scheme implemented in the Phonopy[57]. We use VASP to compute Hellmann-Feynman forces in a supercell. For mono- and few-layer CrI_3 and bilayer $CrCl_3$, the size of the supercell is $2 \times 2 \times 1$ with the corresponding k-grid reduced to $6 \times 6 \times 1$; for bulk CrI_3, the size of the supercell is $2 \times 2 \times 1$ with the corresponding k-grid reduced to $6 \times 6 \times 3$; for bilayer $MnBi_2Te_4$, the supercell size is $3 \times 3 \times 1$ with the corresponding k-grid reduced to $4 \times 4 \times 1$; for bulk $MnBi_2Te_4$, the supercell size is $3 \times 3 \times 1$ with the corresponding k-grid reduced to $4 \times 4 \times 3$. The choice of the supercell size is to ensure at least 10 Å in every lattice direction to avoid interactions between the neighboring cells. We introduce both positive and negative atomic displacements ($\Delta = 0.03$ Å) to the supercell for static calculations to obtain the forces, which are processed by Phonopy to construct the dynamic matrix whose diagonalization provides phonon frequencies and eigenvectors.

Raman intensity calculations

Finally, Raman intensities are computed within the Placzek approximation[20–22,33,34], as discussed above in the section of "Theory of resonant and magneto-Raman scattering". Basically, one needs to calculate the derivatives of the polarizability tensor with respect to the atomic displacements for obtaining the Raman tensor. For both positive and negative atomic displacements along each direction in the unit cell ($\sigma = 0.03$ Å), the frequency-dependent polarizability tensor is computed by VASP (LOPTICS =. TRUE.), and then the derivatives of the polarizability tensor are obtained via the finite difference approach. The SOC effect with the noncollinear magnetic order has to be turned on during the VASP calculations of the polarizability tensor corresponding to each atomic displacement, in order to fully capture the effects of magnetism on the polarizability tensor, the Raman tensor, and subsequently, the Raman intensity[28,29]. The derivatives of the polarizability tensor, combined with the phonon frequencies and phonon eigenvectors, yield the Raman tensor matrix and, subsequently, the Raman intensity for every phonon mode under a given laser polarization set-up. Since DFT tends to underestimate the band gap and excitation energy, the DFT excitation energy is chosen as 1.20 eV for 1L CrI_3 and 2L-4L CrI_3 under the interlayer AFM state unless mentioned otherwise. For 2L-4L CrI_3 under the interlayer FM state, the electronic band structures are changed, as evidenced by the fact that the band gaps are different from the ones under the AFM state by about 0.1–0.14 eV, and hence the DFT excitation energy is correspondingly changed to 1.30 eV. The DFT excitation energy is set as 1.62 eV for $MnBi_2Te_4$.

Data availability

The data that support the plots within this paper and other findings of this study are available from corresponding authors upon reasonable request.

Code availability

Upon request, authors will make available any previously unreported computer code or algorithm used to generate results that are reported in the paper and central to its claims.

Received: 25 June 2024; Accepted: 11 November 2024;
Published online: 19 December 2024

References

1. Huang, B. et al. Layer-dependent ferromagnetism in a van der Waals crystal down to the monolayer limit. *Nature* **546**, 270 (2017).
2. Gong, C. et al. Discovery of intrinsic ferromagnetism in two-dimensional van der Waals crystals. *Nature* **546**, 265 (2017).
3. Burch, K. S., Mandrus, D. & Park, J.-G. Magnetism in two-dimensional van der Waals materials. *Nature* **563**, 47 (2018).
4. Gong, C. & Zhang, X. Two-dimensional magnetic crystals and emergent heterostructure devices. *Science* **363**, eaav4450 (2019).
5. Sivadas, N., Okamoto, S., Xu, X., Fennie, C. J. & Xiao, D. Stacking-dependent magnetism in bilayer CrI_3. *Nano Lett.* **18**, 7658 (2018).
6. Kong, X., Yoon, H., Han, M. J. & Liang, L. Switching interlayer magnetic order in bilayer cri3 by stacking reversal. *Nanoscale* **13**, 16172 (2021).
7. Jiang, S., Shan, J. & Mak, K. F. Electric-field switching of two-dimensional van der Waals magnets. *Nat. Mater.* **17**, 406 (2018).
8. Huang, B. et al. Electrical control of 2d magnetism in bilayer CrI_3. *Nat. Nanotechnol.* **13**, 544 (2018).
9. Huang, B. et al. Tuning inelastic light scattering via symmetry control in the two-dimensional magnet CrI_3. *Nat. Nanotechnol.* **15**, 212 (2020).
10. Sun, Z. et al. Giant nonreciprocal second-harmonic generation from antiferromagnetic bilayer CrI_3. *Nature* **572**, 497 (2019).
11. McCord, J. Progress in magnetic domain observation by advanced magneto-optical microscopy. *J. Phys. D Appl. Phys.* **48**, 333001 (2015).
12. Akbar, A., Khalid, M. W. & Anwar, M. S. Low temperature Voigt effect in the terbium gallium garnet crystal. *Opt. Express* **25**, 30550 (2017).
13. Guo, G., Bi, G., Cai, C. & Wu, H. Effects of external magnetic field and out-of-plane strain on magneto-optical kerr spectra in CrI_3 monolayer. *J. Phys. Condens. Matter* **30**, 285303 (2018).
14. Kumar Gudelli, V. & Guo, G.-Y. Magnetism and magneto-optical effects in bulk and few-layer CrI_3: a theoretical GGA+ U study. *New J. Phys.* **21**, 053012 (2019).
15. Wu, M., Li, Z., Cao, T. & Louie, S. G. Physical origin of giant excitonic and magneto-optical responses in two-dimensional ferromagnetic insulators. *Nat. Commun.* **10**, 2371 (2019).
16. Lee, J.-U. et al. Ising-type magnetic ordering in atomically thin $FePS_3$. *Nano Lett.* **16**, 7433 (2016).
17. Kim, K. et al. Suppression of magnetic ordering in xxz-type antiferromagnetic monolayer $NiPS_3$. *Nat. Commun.* **10**, 345 (2019).
18. Kim, K., Lee, J.-U. & Cheong, H. Raman spectroscopy of two-dimensional magnetic van der Waals materials. *Nanotechnology* **30**, 452001 (2019).
19. Sun, Y.-J., Pang, S.-M. & Zhang, J. Review of Raman spectroscopy of two-dimensional magnetic van der Waals materials. *Chin. Phys. B* **30**, 117104 (2021).
20. Umari, P., Pasquarello, A. & Dal Corso, A. Raman scattering intensities in α-quartz: a first-principles investigation. *Phys. Rev. B* **63**, 094305 (2001).
21. Liang, L. & Meunier, V. First-principles Raman spectra of MoS_2, WS_2 and their heterostructures. *Nanoscale* **6**, 5394 (2014).
22. del Corro, E. et al. Atypical exciton–phonon interactions in WS_2 and WSE_2 monolayers revealed by resonance Raman spectroscopy. *Nano Lett.* **16**, 2363 (2016).
23. Jin, W. et al. Tunable layered magnetism assisted magneto-raman effect in a two-dimensional magnet CrI_3. *Proc. Natl Acad. Sci. USA* **117**, 24664 (2020).

24. McCreary, A. et al. Distinct magneto-Raman signatures of spin-flip phase transitions in CrI_3. *Nat. Commun.* **11**, 3879 (2020).
25. Zhang, Y. et al. Magnetic order-induced polarization anomaly of Raman scattering in 2d magnet CrI_3. *Nano Lett.* **20**, 729 (2019).
26. Lyu, B. et al. Probing the ferromagnetism and spin wave gap in VI_3 by helicity-resolved Raman spectroscopy. *Nano Lett.* **20**, 6024 (2020).
27. Staros, D. et al. A combined first principles study of the structural, magnetic, and phonon properties of monolayer CrI_3. *J. Chem. Phys.* **156**, 014707 (2022).
28. Lei, M. & Coh, S. Large cross-polarized raman signal in CrI_3: a first-principles study. *Phys. Rev. Mater.* **5**, 025202 (2021).
29. Liu, S., Long, M.-Q. & Wang, Y.-P. Theoretical investigations on the magneto-Raman effect of CrI_3. *Phys. Rev. B* **108**, 184414 (2023).
30. Li, J. et al. Intrinsic magnetic topological insulators in van der Waals layered mnbi2te4-family materials. *Sci. Adv.* **5**, eaaw5685 (2019).
31. Deng, Y. et al. Quantum anomalous hall effect in intrinsic magnetic topological insulator $MnBi_2Te_4$. *Science* **367**, 895 (2020).
32. Ahn, J., Kang, S.-H., Yoon, M., Ganesh, P. & Krogel, J. T. Stacking faults and topological properties in $MnBi_2Te_4$: reconciling gapped and gapless states. *J. Phys. Chem. Lett.* **14**, 9052 (2023).
33. Miranda, H. P. et al. Quantum interference effects in resonant Raman spectroscopy of single-and triple-layer $MoTe_2$ from first-principles. *Nano Lett.* **17**, 2381 (2017).
34. Talirz, L. et al. On-surface synthesis and characterization of 9-atom wide armchair graphene nanoribbons. *ACS Nano* **11**, 1380 (2017).
35. Gajdovs, M., Hummer, K., Kresse, G., Furthmuller, J. & Bechstedt, F. Linear optical properties in the projector-augmented wave methodology. *Phys. Rev. B* **73**, 045112 (2006).
36. Loudon, R. The Raman effect in crystals. *Adv. Phys.* **13**, 423 (1964).
37. Ribeiro, H. B. et al. Unusual angular dependence of the Raman response in black phosphorus. *ACS Nano* **9**, 4270 (2015).
38. Dillon Jr, J. & Olson, C. Magnetization, resonance, and optical properties of the ferromagnet CrI_3. *J. Appl. Phys.* **36**, 1259 (1965).
39. McGuire, M. A., Dixit, H., Cooper, V. R. & Sales, B. C. Coupling of crystal structure and magnetism in the layered, ferromagnetic insulator CrI_3. *Chem. Mater.* **27**, 612 (2015).
40. Zhang, W.-B., Qu, Q., Zhu, P. & Lam, C.-H. Robust intrinsic ferromagnetism and half semiconductivity in stable two-dimensional single-layer chromium trihalides. *J. Mater. Chem. C* **3**, 12457 (2015).
41. Carvalho, B. R., Malard, L. M., Alves, J. M., Fantini, C. & Pimenta, M. A. Symmetry-dependent exciton-phonon coupling in 2d and bulk MoS_2 observed by resonance Raman scattering. *Phys. Rev. Lett.* **114**, 136403 (2015).
42. Ling, X. et al. Anisotropic electron-photon and electron-phonon interactions in black phosphorus. *Nano Lett.* **16**, 2260 (2016).
43. Mao, N. et al. Direct observation of symmetry-dependent electron–phonon coupling in black phosphorus. *J. Am. Chem. Soc.* **141**, 18994 (2019).
44. Liang, L., Puretzky, A. A., Sumpter, B. G. & Meunier, V. Interlayer bond polarizability model for stacking-dependent low-frequency raman scattering in layered materials. *Nanoscale* **9**, 15340 (2017).
45. Rodriguez-Vega, M., Leonardo, A. & Fiete, G. A. Group theory study of the vibrational modes and magnetic order in the topological antiferromagnet $MnBi_2Te_4$. *Phys. Rev. B* **102**, 104102 (2020).
46. Cho, Y. et al. Phonon modes and Raman signatures of $MnBi_{2n}Te_{3n+1}$ (n = 1, 2, 3, 4) magnetic topological heterostructures. *Phys. Rev. Res.* **4**, 013108 (2022).
47. Kim, H. H. et al. Evolution of interlayer and intralayer magnetism in three atomically thin chromium trihalides. *Proc. Natl Acad. Sci. USA* **116**, 11131 (2019).
48. Cai, X. et al. Atomically thin $CrCl_3$: an in-plane layered antiferromagnetic insulator. *Nano Lett.* **19**, 3993 (2019).
49. Klein, D. R. et al. Enhancement of interlayer exchange in an ultrathin two-dimensional magnet. *Nat. Phys.* **15**, 1255 (2019).
50. Lu, X., Fei, R., Zhu, L. & Yang, L. Meron-like topological spin defects in monolayer crcl3. *Nat. Commun.* **11**, 4724 (2020).
51. Kresse, G. & Furthmüller, J. Efficient iterative schemes for ab initio total-energy calculations using a plane-wave basis set. *Phys. Rev. B* **54**, 11169 (1996).
52. Kresse, G. & Joubert, D. From ultrasoft pseudopotentials to the projector augmented-wave method. *Phys. Rev. B* **59**, 1758 (1999).
53. Perdew, J. P., Burke, K. & Ernzerhof, M. Generalized gradient approximation made simple. *Phys. Rev. Lett.* **77**, 3865 (1996).
54. Grimme, S., Antony, J., Ehrlich, S. & Krieg, H. A consistent and accurate ab initio parametrization of density functional dispersion correction (DFT-D) for the 94 elements H-Pu. *J. Chem. Phys* **132**, 154104 (2010).
55. Klimeš, J., Bowler, D. R. & Michaelides, A. Van der Waals density functionals applied to solids. *Phys. Rev. B* **83**, 195131 (2011).
56. Dudarev, S. L., Botton, G. A., Savrasov, S. Y., Humphreys, C. J. & Sutton, A. P. Electron-energy-loss spectra and the structural stability of nickel oxide: an LSDA+U study. *Phys. Rev. B* **57**, 1505 (1998).
57. Togo, A. & Tanaka, I. First principles phonon calculations in materials science. *Scr. Mater.* **108**, 1 (2015).

Acknowledgements

This research was conducted at the Center for Nanophase Materials Sciences, which is a DOE Office of Science User Facility. X.K. and L.L. used resources from the Compute and Data Environment for Science (CADES) at the Oak Ridge National Laboratory, which is supported by the Office of Science of the U.S. Department of Energy under Contract No. DE-AC05-00OR22725. The authors also used resources from the National Energy Research Scientific Computing Center, a DOE Office of Science User Facility supported by the Office of Science of the U.S. DOE under Contract No. DE-AC02-05CH11231. Notice: This manuscript has been authored by UT-Battelle, LLC under Contract No. DE-AC05-00OR22725 with the U.S. Department of Energy. The United States Government retains and the publisher, by accepting the article for publication, acknowledges that the United States Government retains a non-exclusive, paid-up, irrevocable, world-wide license to publish or reproduce the published form of this manuscript, or allow others to do so, for United States Government purposes. The Department of Energy will provide public access to these results of federally sponsored research in accordance with the DOE Public Access Plan (http://energy.gov/downloads/doe-public-access-plan).

Author contributions

X.K. performed the calculations and analysis. P.G. contributed to data analysis. L.L. conceived and designed the project. All authors contributed to the manuscript writing.

Competing interests

The authors declare no competing interests.

Additional information

Supplementary information The online version contains supplementary material available at https://doi.org/10.1038/s41699-024-00515-3.

Correspondence and requests for materials should be addressed to Xiangru Kong or Liangbo Liang.